JOURNAL OF MAGNETIC RESONANCE **135,** 242–247 (1998)
ARTICLE NO. MN981547

Radial Echo-Planar Imaging

Afonso C. Silva,*,† Emmanuel L. Barbier,*,† Irving J. Lowe,*,‡ and Alan P. Koretsky*,†

*Pittsburgh NMR Center for Biomedical Research and †Department of Biological Sciences, Carnegie Mellon University, Pittsburgh, Pennsylvania 15213; and ‡Department of Physics and Astronomy, University of Pittsburgh, Pittsburgh, Pennsylvania 15260

Received November 25, 1997; revised May 26, 1998

A new ultrafast magnetic resonance imaging pulse sequence named radial echo-planar imaging (rEPI) is introduced. The sequence is based on a modification of the echo-planar imaging (EPI) sequence to scan *k*-space radially, in an attempt to combine the speed of EPI with the benefits of radial sampling. Like in EPI, all the desired lines in *k*-space are scanned consecutively in opposite directions. The unique feature of this new sequence, however, is that the orientation of the readout gradient is incrementally rotated, so that all the echoes are refocused through the center of *k*-space. Therefore, rEPI data are acquired in a polar grid, and image reconstruction can be done either by means of filtered back-projection or by regridding the data to a Cartesian matrix followed by 2D Fourier transform. First results show that rEPI images can be acquired with the same speed and signal-to-noise ratio of EPI images. rEPI images are also shown to be less sensitive to off-resonance effects than EPI images. Further studies are underway to investigate the usefulness of rEPI for spectroscopic imaging and applications affected by motion. © 1998 Academic Press

INTRODUCTION

Among the many ultrafast MRI sequences available today (*1, 2*), echo-planar imaging (EPI) (*3*) is attractive due to its high signal-to-noise ratio (SNR). Among the many applications of EPI (*4*), imaging of the heart (*5, 6*) and of the abdomen (*7*), perfusion mapping (*8–10*), and functional MRI of the human brain (*11–15*) have clearly benefited from the ultrafast scans at high SNR. Echo-planar techniques have also been successfully used for spectroscopic imaging (*16–21*).

EPI samples data according to a Cartesian grid in *k*-space (Fourier imaging—FI). The resulting image is therefore reconstructed by means of a 2D Fourier transform of the *k*-space data. FI trajectories are not necessarily optimal for all applications. In projection reconstruction imaging, for example, *k*-space data are acquired radially and reconstructed by means of a filtered-back-projection (FBP) algorithm. The radial sampling of *k*-space in FBP provides better SNR due to the absence of phase-encoding gradients (*22*). Radial sampling is highly beneficial for reducing motion artifacts due to the intrinsic oversampling of the low spatial frequencies (*23*). FBP techniques are usually less prone to flow-induced artifacts than FI techniques (*24*), and have been extensively used for obtaining chemical-shift information (*16–18, 25, 26*).

To date, FBP techniques have not been performed in a single-shot, ultrafast imaging sequence like EPI. The combination of echo-planar readouts with a polar raster was first proposed by Mansfield (*16*) and later implemented by Doyle and Mansfield (*17*) and by Bowtell *et al.* (*18*). The sequence, designed for fast chemical-shift imaging and named projection-reconstruction echo planar (PREP), consisted of a multipass procedure in which echo-planar readout gradients were used to encode one spatial dimension and one chemical-shift dimension on each pass. To encode the second spatial dimension, the sequence was repeated with the readout gradient oriented at different angles to produce a set of projections of the object.

In this work, we propose a novel single-shot ultrafast MRI sequence, named radial echo-planar imaging (rEPI). rEPI is based on a modification of the EPI sequence to acquire the data according to a polar grid. The *k*-space trajectories in rEPI are similar to those proposed by Ljunggren in (*27*). Like in EPI, rEPI scans lines in *k*-space consecutively in opposite directions. However, the orientation of the readout gradient is incrementally rotated so that all the echoes are refocused through the center of *k*-space. Because the data are acquired in a polar grid, FBP algorithms can be used to reconstruct the image following the proper time reversal of the alternate lines in *k*-space. This Communication describes the rEPI sequence and presents the first experimental results obtained with this new ultrafast MRI technique.

THE rEPI PULSE SEQUENCE

The most basic pulse sequence for rEPI is shown in Fig. 1A. A 90° RF pulse is used with the slice-selective gradient to excite the magnetization from the slice of interest. The resulting transverse magnetization is taken to the extremity of *k*-space along one of the two orthogonal axes, say, to point $(-kx_{\max}, 0)$. Two orthogonal readout gradients are then applied simultaneously to scan *k*-space along consecutive diam-

1090-7807/98 $25.00

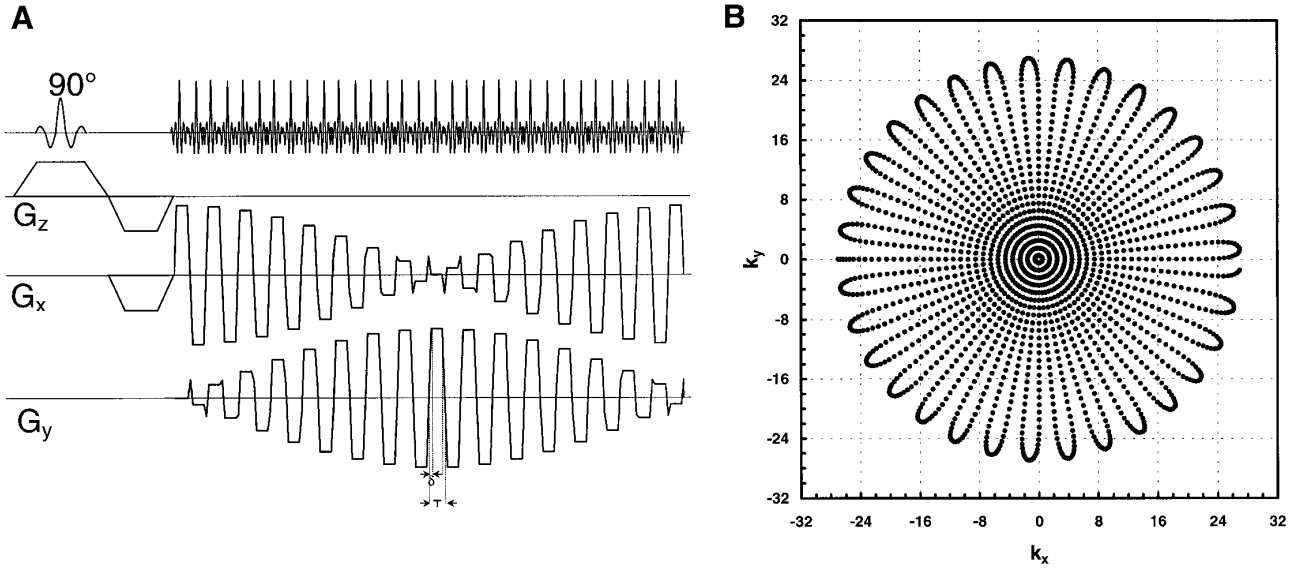

FIG. 1. The single-shot rEPI pulse sequence diagram for 32 projections. (A) For gradient-echo rEPI, a slice-selective 90° RF pulse excites the magnetization into the transverse plane. The readout gradients then scan *k*-space consecutively according to the *k*-space trajectories shown in (B). The rise time δ and the acquisition time per echo T are indicated in (A).

eters (projections). The magnitude of the resulting readout gradient is kept constant, while its orientation is rotated and its sign is reversed at the beginning of each new *k*-space line, so those consecutive projections in *k*-space are scanned in opposing directions. The angle between any two adjacent projections is π/N_p, where N_p is the number of projections acquired. At the end of each projection in *k*-space, the readout gradients bring the magnetization to the beginning of the next projection according to the *k*-space trajectories shown in Fig. 1B. The analytical expressions for the gradient waveforms are as follows:

- during the plateau of the gradients,

$$G_x(t) = G_{ro}\cos(n \cdot \pi/N_p)\cdot(-1)^n, \quad n \cdot T + \delta \le t < (n+1) \cdot T - \delta$$
$$G_y(t) = G_{ro}\sin(n \cdot \pi/N_p)\cdot(-1)^n; \qquad [1]$$

- and, in between two consecutive diameters in *k*-space,

$$G_x(t) = -G_{step}\sin[(n+1/2) \cdot \pi/N_p]\cdot(-1)^n, \quad (n+1) \cdot T - \delta \le t < (n+1) \cdot T + \delta$$
$$G_y(t) = G_{step}\cos[(n+1/2) \cdot \pi/N_p]\cdot(-1)^n, \qquad [2]$$

where N_r is the number of points sampled per projection, T is the acquisition time per echo ($T = N_r$/Bandwidth), δ is the rise time of the gradients, G_{step} is the intensity of the resulting gradient that brings the transverse magnetization from the end of one diameter to the beginning of the following diameter, given by

$$G_{step} = G_{ro} \cdot \sqrt{2 \cdot [1 - \cos(\pi/N_p)]} \cdot \frac{T - \delta}{2 \cdot \delta}, \qquad [3]$$

G_{ro} is the intensity of the resulting readout gradient, given by γG_{ro} = Bandwidth/FOV, and $n = 0, 1, 2, \ldots, N_p - 1$. Reconstruction of the image can be performed using FBP algorithms or by data regridding to a Cartesian *k*-space followed by 2D Fourier transform (i.e., like in Fourier imaging).

It is possible to devise a few variants of the sequence shown in Fig. 1. Like in EPI, many different types of magnetization preparation periods can be introduced into rEPI. For example, to minimize T_2^* effects on the image, the sequence shown in Fig. 1A can also be modified to include a slice-selective 180° RF pulse following the excitation RF pulse to produce a spin echo at the center of the acquisition window. T_1 weighting and diffusion weighting can also be easily incorporated into rEPI. Furthermore, when desired, the sequence can be segmented into N_{seg} pieces. For segmentation, N_p/N_{seg} consecutive projections can be acquired by keeping the original angle between the projections, repeating the process N_{seg} times to complete the image. Another alternative segmentation scheme consists in acquiring *k*-space lines in an interleaved manner by increasing the angle between the projections. Data from the resulting segments should then be shuffled prior to reconstruction. Segmentation can be beneficial when very high spatial resolution is desired and when T_2^* is severely short. As all echoes are refocused through the center of *k*-space, a short T_2^* can intro-

duce an uneven weighting in the data that can lead to severe blurring and distortions in the image. The use of segmentation in this case is recommended to decrease the acquisition time and avoid signal decay due to T_2^*.

RESULTS

Figure 2 shows transverse ^{1}H MR images of a cylindrical water phantom. The image in Fig. 2A was acquired for reference purposes using a conventional spin-echo image with a repetition time TR = 500 ms and reconstructed by means of a 2D FFT algorithm. As expected, the image shows uniform intensity and no geometrical distortions. To test our FBP routine (see details under Experimental), a gradient-echo image of the same slice was acquired using conventional projection-reconstruction gradients and the same repetition time TR = 500 ms and reconstructed using FBP. This image is shown in Fig. 2B. There are no noticeable artifacts in the object, which agrees very well with the spin-echo image in shape as well as in uniform intensity distribution. The background in this image is uniform, confirming the correctness of our reconstruction algorithm.

The EPI image of the same object is shown in Fig. 2C. This image was acquired in 20.48 ms, according to the parameters listed under Experimental. A reference scan acquired without a phase-encoding gradient was used to minimize $N/2$ ghosts (*28*) in the EPI image. This image presents very uniform signal intensity, and almost no geometrical distortions, except for a small shortening along the read direction (vertical direction in Fig. 2C). For the EPI image, the SNR, defined here as the mean signal intensity of an ROI placed over the object divided by the standard deviation of the same ROI placed outside the object (i.e., over the noise) (*29*), was $\mathrm{SNR}_{\mathrm{EPI}} = 139$. Figure 2D shows the corresponding rEPI image, also acquired in 20.48 ms, and reconstructed with the FBP routine. This image agrees very well in geometry with the spin-echo (Fig. 2A) and the gradient-echo (Fig. 2B) images. Signal intensity is also uniform over the object, although some ringing artifacts can be seen, similar to those present in the spin-echo and in the EPI images. The SNR in the rEPI image was $\mathrm{SNR}_{\mathrm{rEPI}} = 123$, smaller than $\mathrm{SNR}_{\mathrm{EPI}}$. This is against the $\sqrt{12/\pi}$ improvement in SNR of FBP techniques over FI techniques predicted in (*22*), and possible reasons for this are presented under Discussion. As it can be clearly seen by comparing the different images in Fig. 2, the rEPI image (Fig. 2D) demonstrates the feasibility of this new ultrafast imaging method.

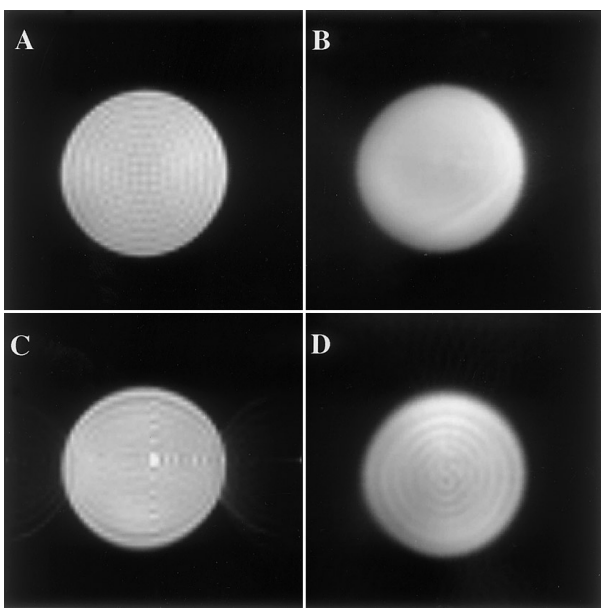

FIG. 2. Axial images of a tube of water. (A) Spin-echo image. (B) Projection-reconstruction gradient-echo image. This image was reconstructed with a FBP algorithm developed in our center. (C) Single-shot EPI image, acquired in 20.48 ms. A reference scan was used to minimize $N/2$ ghosts. (D) Single-shot rEPI image, also acquired in 20.48 ms and reconstructed with the same algorithm used in (B).

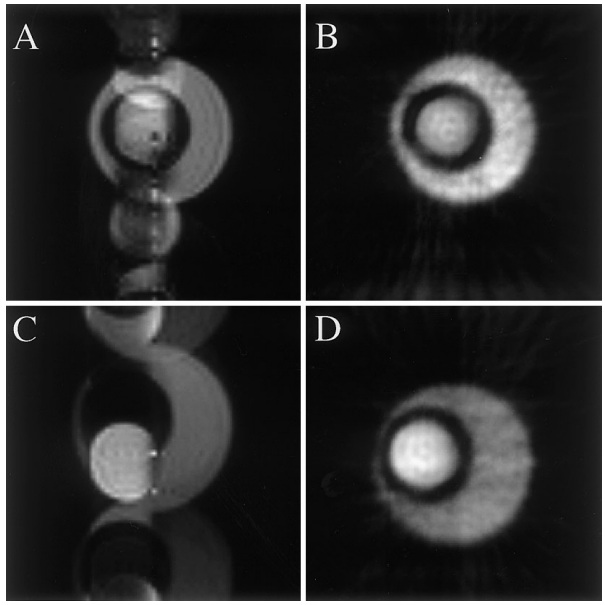

FIG. 3. Comparison of EPI and rEPI for sensitivity to off-resonant effects. Images (A) and (B) are from a test phantom consisting of a small tube of olive oil inside a larger tube of tap water. In the EPI image (A), the olive oil appears as ghosts along the phase-encoding direction. In the rEPI image (B), fat and water preserve their true spatial location, and artifacts appear in the form of blurring and radial streaks. Images (C) and (D) are from a phantom consisting of a tube of lactic acid immersed in a tube of olive oil. The spectrometer frequency was set to the water frequency, so that in the EPI image (C) neither fat nor lactate appears at their true locations. In the rEPI image (D), water, lactate, and fat appear at their true spatial locations.

To test the sensitivity of rEPI to off-resonant effects, images of a water–fat phantom and of a water–fat–lactate phantom were acquired. These images are shown in Fig. 3. Figure 3A shows the EPI image, and Fig. 3B shows the corresponding rEPI image of a phantom consisting of an inner tube of olive oil and an outer tube of tap water. In EPI (Fig. 3A), the olive oil tube appears out of its true location due to the off-resonance

artifacts that greatly affect EPI images (*30*). These artifacts appear as ghosts along the phase-encoding direction, as shown in Fig. 3A. In the rEPI image (Fig. 3B), the artifacts due to the off-resonance frequency of fat are much less severe. In this image, fat and water are represented at their correct location. The effects of the off-resonant fat signal are to cause blurring of the object, and also streaks that move away from the object and therefore do not degrade the quality of the image. Similar results can be observed in Fig. 3C and Fig. 3D. Figure 3D shows the EPI image of a phantom consisting of a tube of lactic acid immersed inside a tube of olive oil. The spectrometer frequency was set to the water frequency, so that neither lactate nor fat is on resonance in that image. In the rEPI image shown in Fig. 3D, water, lactate, and fat appear at their true spatial locations, and the off-resonance artifacts appear in the form of image blurring and streaks that move toward outside the object.

DISCUSSION

The EPI technique allows the generation of MR images within times typically less than 100 ms, at very high SNR. This very powerful combination of ultrafast scans at high SNR makes EPI very attractive for a number of applications both in clinical and in research MRI. Because of this, EPI is becoming more and more an indispensable tool. It is well known, however, that EPI suffers from a number of image artifacts that degrade image quality and limits its range of applications (*30*). Besides being very demanding on hardware and in particular on gradient technology, EPI is very sensitive to off-resonance effects, especially those caused by susceptibility differences and by field inhomogeneities. The purpose of this work is to investigate an alternative ultrafast MRI technique that preserves the powerful speed–SNR combination of EPI while improving on image quality.

The particular choice of *k*-space trajectories for a given MRI method determines the efficiency with which the image information at each spatial frequency is acquired (*31*). From this point of view radial sampling of *k*-space is very attractive (*22*). The rEPI sequence proposed here attempts to combine the advantages of projection-reconstruction imaging with ultrafast scanning of *k*-space. The pulse sequence diagram shown in Fig. 1 shows the readout gradient waveforms for 32 projections. It is easy to realize the importance of both G_x and G_y gradients having very similar performances in terms of rise time, stability, and eddy-current compensation to produce the intended *k*-space trajectories shown in Fig. 1B. Any asymmetry in gradient performance will prevent the projections from all crossing at the center of *k*-space, and will therefore introduce blurring and artifacts in the rEPI image. The exact *k*-space trajectories produced by the gradient waveforms can be accurately measured using *k–t* trajectory probing techniques (*32*). Measurement of the actual *k*-space trajectories allows for the assessment of any deviations from the intended trajectories, and enables the proper regridding and reconstruction of the data. In spectrometers that have asymmetric performance of the readout gradients, it is very likely that rEPI will benefit from the use of these *k–t* trajectory probing techniques. The rEPI image shown in Fig. 2D compares very well in geometry and uniformity with the corresponding spin-echo, gradient-echo, and EPI images. However, the SNR of this rEPI image was about 11% smaller than the SNR of the corresponding EPI image. We believe that this is due to eddy currents generated in our volume RF coil when playing the readout gradients. Since EPI has only one readout gradient direction, it is likely that less eddy currents are generated with EPI than with rEPI. This problem can be minimized with a balanced eddy-current compensation scheme, and with the use of surface RF coils that are immune to induced eddy currents.

As it can be seen from the images in Fig. 3, rEPI is less sensitive to off-resonance effects than EPI. Artifacts in rEPI are seen in the form of blurring and streaks that move away from the object, while in EPI the off resonance gets spread out along the phase-encoding direction. While both EPI and rEPI images shown in Fig. 3 are affected by off-resonance artifacts, the rEPI images are rendered more useful because true spatial location is preserved in those images. This most likely occurs because phase modulations of the projections due to chemical shift are minimized when magnitude calculations are performed prior to FBP (see Experimental). The FBP algorithm used here does not use phase information to reconstruct the object. This is opposed to EPI where phases induced by the gradients and by chemical shift cannot be separated in a single shot (*30*).

A point which is worthwhile mentioning in this paper and which will be the object of further studies is that, in rEPI, the magnetization is always refocused through the center of *k*-space, which is therefore sampled N_p times, at times $t = T/2$, $3T/2$, $5T/2$, . . . , $N_pT/2$, when an odd number of points along the read direction is acquired. Therefore, for the rEPI sequence, the transverse magnetization acquired at the origin of *k*-space is modulated by chemical-shift dephasing only. Taking the Fourier transform of the N_p central *k*-space points should yield the chemical-shift spectrum of the sample with a bandwidth of $1/T$. We are currently working to determine how useful this information will be in using rEPI for spectroscopic imaging.

CONCLUSIONS

The results presented here prove that it is possible to combine the speed and SNR of EPI with the advantages of radial sampling, namely the oversampling of low spatial frequencies. This approach has been used before in spiral imaging (*33*), and it will certainly be very interesting to compare spiral imaging with rEPI in future work. Radial echo-planar images were acquired in 20.48 ms with a SNR comparable to that of the corresponding EPI images. rEPI also proved to be less sensitive to off-resonance effects by preserving the correct spatial

location of the off-resonant species. Provided that it is implemented in a spectrometer that has well-balanced gradients, rEPI is likely to become a very attractive ultrafast MRI sequence.

EXPERIMENTAL

All experiments were performed on a Bruker 7.0-T/15-cm AVANCE spectrometer equipped with a 4-cm-diameter shielded microimaging gradient set capable of generating 50 G/cm with a rise time of 50 μs. EPI and rEPI images were acquired using the spin-echo approach, using a 64×64 matrix, FOV = 2.56 cm, slice thickness = 2 mm, TE = 27 ms (from middle of 90° RF pulse to center of acquisition window), and acquisition bandwidth of 200 kHz (acquisition time per echo $T = 320$ μs). The total image acquisition time was 20.48 ms. EPI reference images were acquired by removing the phase-encoding gradient and used to reconstruct the EPI images without $N/2$ ghosts (*32*). A MATLAB (The Mathworks Inc., MA) simulation program was used to generate the gradient waveforms for rEPI shown in Fig. 1A and to calculate the resulting *k*-space trajectories shown in Fig. 1B.

The rEPI images were reconstructed by means of a FBP algorithm developed in our center, without use of reference images. Prior to the FBP algorithm per say, the acquired data were corrected for DC offsets in the baseline and every other echo was time-reversed. This algorithm consisted of five basic steps:

(i) A 1D FFT of the data was taken for each projection to obtain the profile of the object along the orientation of the gradients.

(ii) The magnitude of each resulting profile was inverse Fourier transformed back to *k*-space.

(iii) Each projection was multiplied by a ramp function of the kind $|\mathbf{k}|$.

(iv) These filtered projections were 1D Fourier transformed to obtain the filtered profiles.

(v) The filtered profiles were back-projected, resulting in the image.

To test the sensitivity of rEPI to off-resonance artifacts, two test phantoms were prepared. The first phantom consisted of a small tube of olive oil inside a larger tube filled with tap water. For this phantom, two proton resonance frequencies should be observed: the water resonance, and the lipid resonance, which at 7 T is shifted by approximately 1025 Hz from water. The second phantom consisted of a small tube containing lactic acid inside a larger tube filled with olive oil. For this phantom, lactic acid resonates at 209 Hz (quartet) and 1050 Hz (doublet) with respect to the water peak.

ACKNOWLEDGMENTS

The authors acknowledge Dr. Xiaoping Hu for helpful discussions during the preparation of the manuscript. This work was supported by an NIH Research Resource Award (RR-03631) and an NIH Research Career Development Award (HL-02847) to A.P.K. Financial support for the establishment of the Pittsburgh NMR Center for Biomedical Research was provided by the Richard King Mellon Foundation, the Lucille Markey Charitable Trust, the Ralph M. Parsons Foundation, and the Ben Franklin Partnership Program of the Commonwealth of Pennsylvania.

REFERENCES

1. M. S. Cohen and R. M. Weisskoff, Ultra-fast imaging, *Magn. Reson. Imaging* **9,** 1–37 (1991).
2. A. C. Silva and I. J. Lowe, Ultra-fast magnetic resonance imaging sequences, *Brazilian J. Phys.* **25,** 404–416 (1995).
3. P. Mansfield, Multi-planar image formation using NMR spin echoes, *J. Phys. C (Solid State Phys.)* **10,** L55–L58 (1977).
4. M. K. Stehling, R. Turner, and P. Mansfield, Echo-planar imaging: Magnetic resonance imaging in a fraction of a second, *Science* **254,** 43–50 (1991).
5. C. P. Davis, G. C. McKinnon, J. F. Debatin, D. Leben, A. C. Eichenberger, S. Duewell, and G. K. von Schulthess, Normal heart: Evaluation with echo-planar MR imaging, *Radiology* **191,** 691–696 (1994).
6. H. J. Lamb, J. Doornbos, E. A. van der Velde, M. C. Kruit, J. H. Reiber, and A. de Roos, Echo planar MRI of the heart on a standard system: Validation of measurements of left ventricular function and mass, *J. Comput. Assist. Tomogr.* **20,** 942–949 (1996).
7. M. F. Muller and R. R. Edelman, Echo planar imaging of the abdomen, *Top. Magn. Reson. Imaging* **7,** 112–119 (1995).
8. R. R. Edelman, B. Siewert, D. G. Darby, V. Thangaraj, A. C. Nobre, M. M. Mesulam, and S. Warach, Qualitative mapping of cerebral blood flow and functional localization with echo-planar MR imaging and signal targeting with alternating radio frequency, *Radiology* **192,** 513–520 (1994).
9. S. G. Kim, Quantification of relative cerebral blood flow change by flow-sensitive alternating inversion recovery (FAIR) technique: Application to functional mapping, *Magn. Reson. Med.* **34,** 293–301 (1995).
10. F. Q. Ye, J. Pekar, P. Jezzard, J. H. Duyn, J. A. Frank, and A. C. McLaughlin, Perfusion imaging of the human brain at 1.5 T using a single-shot EPI spin tagging approach, *Magn. Reson. Med.* **36,** 219–224 (1996).
11. K. K. Kwong, Functional magnetic resonance imaging with echo planar imaging, *Magn. Reson. Q.* **11,** 1–20 (1995).
12. R. S. Menon, S. Ogawa, X. Hu, J. P. Strupp, P. Anderson, and K. Ugurbil, BOLD based functional MRI at 4 Tesla includes a capillary bed contribution: Echo-planar imaging correlates with previous optical imaging using intrinsic signals, *Magn. Reson. Med.* **33,** 453–459 (1995).
13. D. Le Bihan, Functional MRI of the brain principles, applications and limitations, *J. Neuroradiol.* **23,** 1–5 (1996).
14. X. Hu, T. H. Le, and K. Ugurbil, Evaluation of the early response in fMRI in individual subjects using short stimulus duration, *Magn. Reson. Med.* **37,** 877–884 (1997).
15. Y. Yang, V. S. Mattay, D. R. Weinberger, J. A. Frank, and J. H. Duyn, Localized echo-volume imaging methods for functional MRI, *J. Magn. Reson. Imaging* **7,** 371–375 (1997).
16. P. Mansfield, Spatial mapping of the chemical shift in NMR, *J. Phys. D (Appl. Phys.)* **16,** L235–L238 (1983).
17. M. Doyle and P. Mansfield, Chemical-shift imaging: A hybrid approach. *Magn. Reson. Med.* **5,** 255–261 (1987).

18. R. Bowtell, M. G. Cawley, and P. Mansfield, Proton chemical-shift mapping using PREP, *J. Magn. Reson.* **82,** 634–639 (1989).

19. D. N. Guilfoyle, A. Blamire, B. Chapman, R. J. Ordidge, and P. Mansfield, PEEP—A rapid chemical-shift imaging method, *Magn. Reson. Med.* **10,** 282–287 (1989).

20. S. Posse, G. Tedeschi, R. Risinger, R. Ogg, and D. Le Bihan, High speed ^{1}H spectroscopic imaging in human brain by echo planar spatial–spectral encoding, *Magn. Reson. Med.* **33,** 34–40 (1995).

21. G. Metzger and X. Hu, Application of interlaced Fourier transform to echo-planar spectroscopic imaging, *J. Magn. Reson.* **125,** 166–170 (1997).

22. P. T. Callaghan and C. D. Eccles, Sensitivity and resolution in NMR imaging, *J. Magn. Reson.* **71,** 426–445 (1987).

23. G. H. Glover and J. M. Pauly, Projection reconstruction techniques for reduction of motion effects in MRI, *Magn. Reson. Med.* **28,** 275–289 (1992).

24. D. G. Nishimura, J. I. Jackson, and J. M. Pauly, On the nature and reduction of the displacement artifact in flow images, *Magn. Reson. Med.* **22,** 481–492 (1991).

25. W. B. Hyslop, R. K. Woods, and P. C. Lauterbur, Four-dimensional spectral–spatial imaging using projection reconstruction, *IEEE Trans. Med. Imaging* **14,** 374–383 (1995).

26. M. Meininger, P. M. Jakob, M. von Kienlin, D. Koppler, G. Bringmann, and A. Haase, Radial spectroscopic imaging, *J. Magn. Reson.* **125,** 325–331 (1997).

27. S. Ljunggren, A simple graphical representation of Fourier-based imaging methods, *J. Magn. Reson.* **54,** 338–343 (1983).

28. H. Bruder, H. Fischer, H. E. Reinfelder, and F. Schmitt, Image reconstruction for echo planar imaging with nonequidistant *k*-space sampling, *Magn. Reson. Med.* **23,** 311–323 (1992).

29. R. M. Henkelman, Measurement of signal intensities in the presence of noise in MR images, *Med. Phys.* **12,** 232–233 (1985).

30. F. Farzaneh, S. J. Riederer, and N. J. Pelc, Analysis of T2 limitations and off-resonance effects on spatial resolution and artifacts in echo-planar imaging, *Magn. Reson. Med.* **14,** 123–139 (1990).

31. D. B. Twieg, The *k*-trajectory formulation of the NMR imaging process with applications in analysis and synthesis of imaging methods, *Med. Phys.* **10,** 610–621 (1983).

32. G. F. Mason, T. Harshbarger, H. P. Hetherington, Y. Zhang, G. M. Pohost, and D. B. Twieg, A method to measure arbitrary *k*-space trajectories for rapid MR imaging, *Magn. Reson. Med.* **38,** 492–496 (1997).

33. C. B. Ahn, J. H. Kim, and Z. H. Cho, High-speed spiral-scan echo planar NMR imaging, *IEEE Trans. Med. Imaging* **MI-5,** 2–7 (1986).